Direct Measurement of the Spectral Structure of Cosmic-Ray Electrons+Positrons in the TeV Region with CALET on the International Space Station

Supplemental material relative to "Direct Measurement of the Spectral Structure of Cosmic-Ray Electrons+Positrons in the TeV region with CALET on the International Space Station"

BDT RESPONSE DISTRIBUTION

Figure S1 presents the BDT response (R_{BDT}) distributions in the $949 < E < 1504$ GeV (top) and $1504 < E < 4755$ GeV (bottom) bins including all acceptance conditions [S1]. While there are noticeable discrepancies in the $-0.2 < R_{BDT} < 0.3$ region, their possible effects to the resultant spectrum are included in the systematic uncertainty relative to the BDT stability.

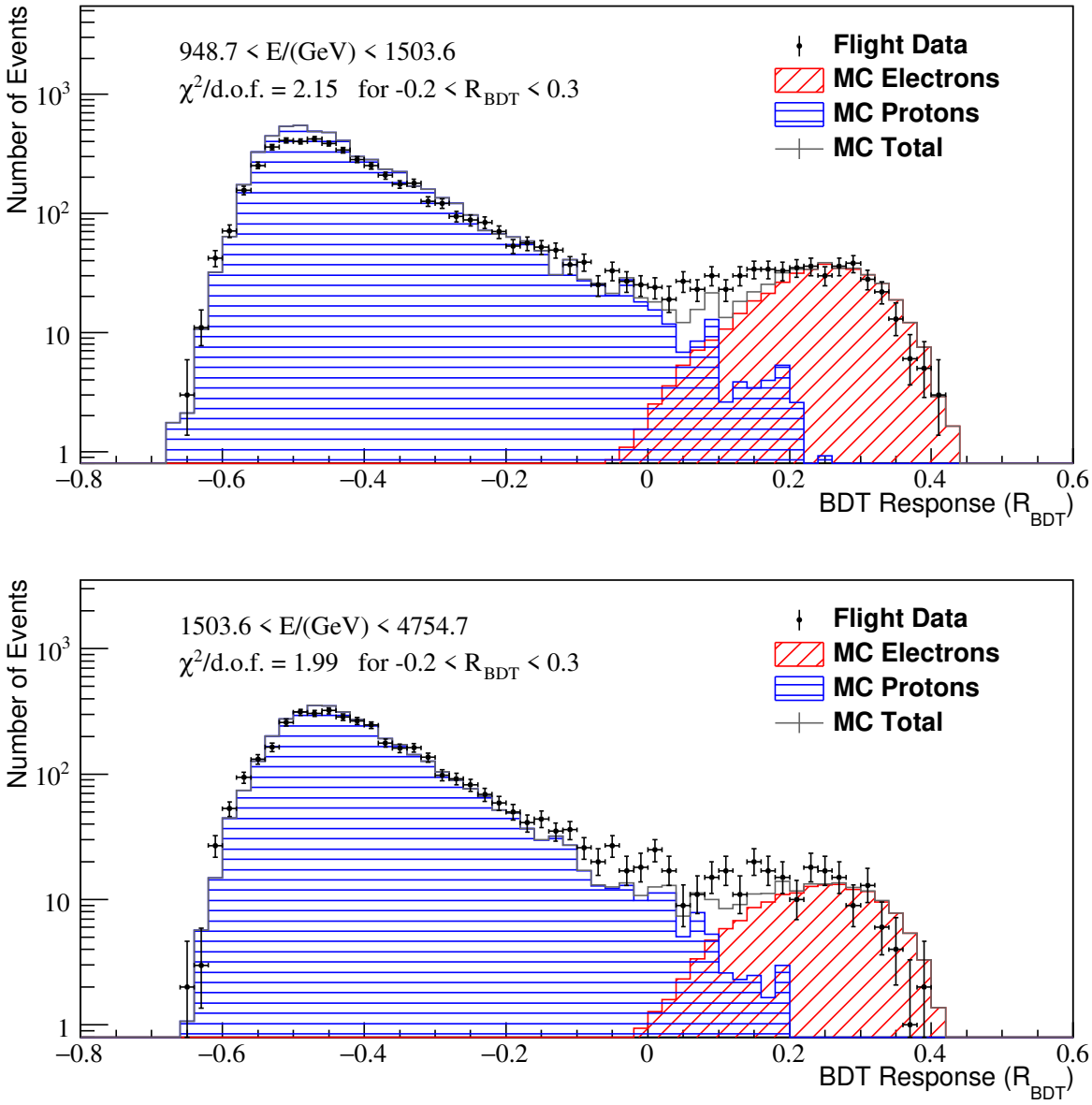

FIG. S1. BDT distribution in $949 < E < 1504$ GeV (top) and $1504 < E < 4755$ GeV(bottom) bins.

SYSTEMATIC UNCERTAINTIES

Figure S2 shows the energy dependence of systematic uncertainties in the tracking algorithms (Electromagnetic shower tracking vs combinatorial Kalman filter tracking), charge selction methods (CHD vs IMC), electron identification methods (K-estimator vs BDT) and MC models (Geant4 vs EPICS). The data points are fitted with log-polynomial functions to mitigate the effect of statistical fluctuations while preserving possible energy dependent structures. Fit functions are shown as curves and are used to estimate energy dependent systematic uncertainties. These resultant functions are used to quote the systematic uncertainty considering the sign of the difference between implemented and comparison method in each energy bin. The K-estimator is not appropriate at high energies due to the increasing background, therefore the function is extrapolated as constant maximum above the fit range.

BDT stability is evaluated from the stability of the flux obtained with 100 independent training samples as a function of BDT cut efficiency in the range from 70% to 90% in 1% steps for each corresponding test sample. The energy dependence of the BDT stability is shown in Fig. S3.

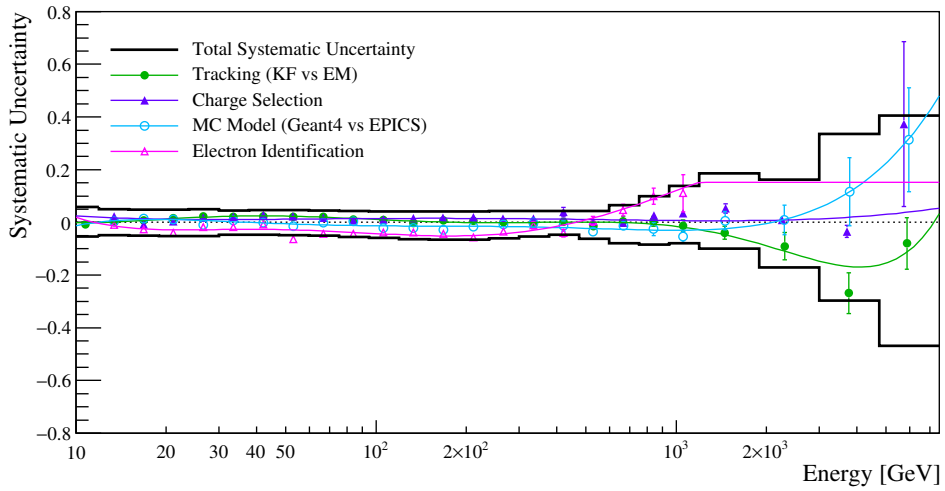

FIG. S2. Energy dependence of systematic uncertainties. The solid line represents the total systematic. See text for details.

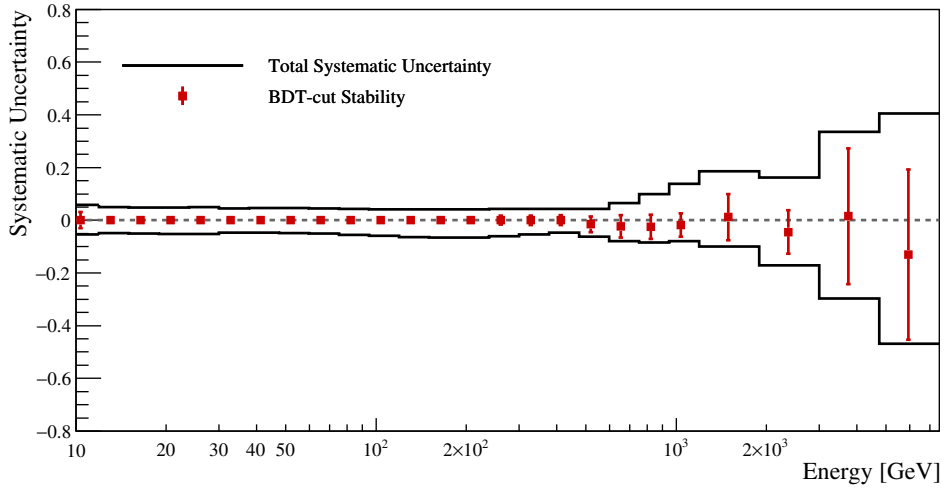

FIG. S3. Energy dependence of systematic uncertainties. The red squares represent the average of all BDT training samples with respect to the standard 80% efficiency case, while error bars represent the standard deviation at each energy bin. The upper and lower edge of the error bars are taken as the total systematic uncertainty due to the BDT analysis.

ENLARGED FIGURE OF ALL-ELCTRON SPECTUM OF CALET

The electron and positron spectrum measured by CALET (red circles) is shown in Fig. S4 where it is compared with the experimental results of AMS-02 [S3], Fermi-LAT [S4], and DAMPE [S5]. The hatched band shows the total uncertainty for CALET.

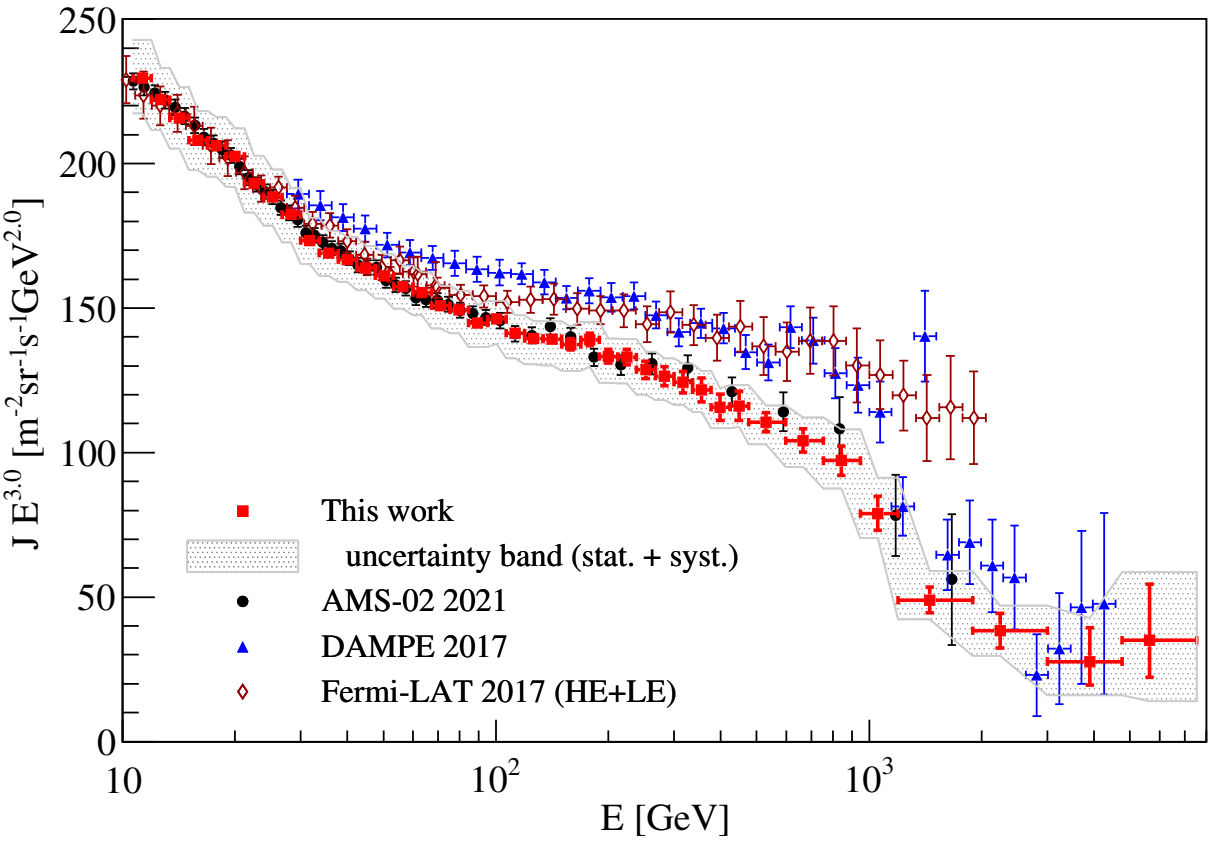

FIG. S4. Cosmic-ray electron + positron spectrum observed with CALET from 10.6 GeV to 7.5 TeV, compared with other direct measurements. The horizontal error bars are representative of the bin width.

TABLE I. Table of CALET electron plus positron spectrum. Mean energy is calculated using the candidate events in the energy bin. For the flux, the first and second errors represent the statistical uncertainties (68 % confidence level) and systematic uncertainties, respectively. Detailed breakdown of systematic errors is included where $\sigma_{\rm BDT}$, $\sigma_{\rm trig.}$, $\Delta_{\rm norm.}$, $\Delta_{\rm trk.}$, $\Delta_{\rm chg.}$, $\Delta_{\rm ID}$ and $\Delta_{\rm MC}$ denote systematic errors due to BDT stability, trigger, absolute normalization, tracking, charge identification, electron identification, and MC model dependence, respectively. While the first two components must be added in quadrature to the statistical errors in a spectral analysis, the latter five contributions could be treated by introducing weight factors corresponding to each component as fitted nuisance parameters. This constrains the possible correction to the fit function from each component to a shift with the already determined energy dependence (or non-dependence). The likelihood of the correction from each component enters into the fit quality by adding the squared weight factor of each component to the χ^2. Although $\Delta_{\rm norm.}$ can be ignored in a spectral study using only CALET data, such as the fits shown in Figs. 3 and S5 , it should also be treated as a nuisance parameter in a combined analysis with the positron spectrum.

Energy Bin	Mean Energy	Flux	Systematic Uncertainties (relative to flux)						
(GeV)	(GeV)	($\mathrm{m^{-2}sr^{-1}s^{-1}GeV^{-1}}$)	$\sigma_{\rm BDT}$	$\sigma_{\rm trig.}$	$\Delta_{\rm norm.}$	$\Delta_{\rm trk.}$	$\Delta_{\rm chg.}$	$\Delta_{\rm ID}$	$\Delta_{\rm MC}$
10.6–11.9	11.3	$(1.599 \pm 0.002\,^{+0.091}_{-0.085}) \times 10^{-1}$	0.031	0.024	0.036	-0.001	0.021	0.002	-0.003
11.9–13.4	12.6	$(1.099 \pm 0.002\,^{+0.055}_{-0.052}) \times 10^{-1}$	0.015	0.024	0.036	0.000	0.018	-0.009	0.004
13.4–15.0	14.2	$(7.575 \pm 0.013\,^{+0.374}_{-0.373}) \times 10^{-2}$	0.015	0.024	0.036	0.003	0.016	-0.018	0.008
15.0–16.9	15.9	$(5.166 \pm 0.010\,^{+0.248}_{-0.259}) \times 10^{-2}$	0.009	0.024	0.036	0.006	0.014	-0.023	0.010
16.9–18.9	17.8	$(3.628 \pm 0.007\,^{+0.176}_{-0.187}) \times 10^{-2}$	0.009	0.024	0.036	0.009	0.013	-0.026	0.011
18.9–21.2	20.0	$(2.524 \pm 0.006\,^{+0.123}_{-0.132}) \times 10^{-2}$	0.008	0.024	0.036	0.012	0.012	-0.028	0.011
21.2–23.8	22.5	$(1.706 \pm 0.004\,^{+0.084}_{-0.090}) \times 10^{-2}$	0.008	0.024	0.036	0.016	0.011	-0.028	0.010
23.8–26.7	25.2	$(1.177 \pm 0.003\,^{+0.059}_{-0.062}) \times 10^{-2}$	0.009	0.024	0.036	0.018	0.011	-0.028	0.008
26.7–30.0	28.3	$(8.076 \pm 0.018\,^{+0.408}_{-0.422}) \times 10^{-3}$	0.009	0.024	0.036	0.021	0.011	-0.028	0.006
30.0–33.7	31.7	$(5.433 \pm 0.014\,^{+0.246}_{-0.252}) \times 10^{-3}$	0.010	0.000	0.036	0.023	0.011	-0.027	0.004
33.7–37.8	35.6	$(3.747 \pm 0.011\,^{+0.172}_{-0.173}) \times 10^{-3}$	0.010	0.000	0.036	0.024	0.011	-0.027	0.001
37.8–42.4	39.9	$(2.620 \pm 0.009\,^{+0.121}_{-0.122}) \times 10^{-3}$	0.011	0.000	0.036	0.024	0.011	-0.027	-0.001
42.4–47.5	44.8	$(1.821 \pm 0.007\,^{+0.085}_{-0.085}) \times 10^{-3}$	0.011	0.000	0.036	0.024	0.012	-0.027	-0.003
47.5–53.3	50.3	$(1.268 \pm 0.005\,^{+0.059}_{-0.060}) \times 10^{-3}$	0.012	0.000	0.036	0.024	0.012	-0.028	-0.006
53.3–59.9	56.4	$(8.778 \pm 0.042\,^{+0.402}_{-0.428}) \times 10^{-4}$	0.012	0.000	0.036	0.022	0.012	-0.030	-0.007
59.9–67.2	63.3	$(6.122 \pm 0.033\,^{+0.276}_{-0.308}) \times 10^{-4}$	0.012	0.000	0.036	0.021	0.013	-0.032	-0.009
67.2–75.4	71.0	$(4.213 \pm 0.026\,^{+0.187}_{-0.220}) \times 10^{-4}$	0.012	0.000	0.036	0.018	0.013	-0.034	-0.011
75.4–84.6	79.7	$(2.953 \pm 0.021\,^{+0.129}_{-0.160}) \times 10^{-4}$	0.012	0.000	0.036	0.016	0.014	-0.037	-0.012
84.6–94.9	89.4	$(2.027 \pm 0.016\,^{+0.087}_{-0.114}) \times 10^{-4}$	0.012	0.000	0.036	0.014	0.014	-0.040	-0.012
94.9–106.4	100.4	$(1.45 \pm 0.01\,^{+0.06}_{-0.08}) \times 10^{-4}$	0.012	0.000	0.036	0.011	0.015	-0.043	-0.013
106.4–119.4	112.5	$(9.92 \pm 0.10\,^{+0.42}_{-0.60}) \times 10^{-5}$	0.012	0.000	0.036	0.008	0.015	-0.045	-0.014
119.4–134.0	126.3	$(6.93 \pm 0.08\,^{+0.29}_{-0.44}) \times 10^{-5}$	0.013	0.000	0.036	0.006	0.015	-0.048	-0.014
134.0–150.4	141.7	$(4.90 \pm 0.06\,^{+0.20}_{-0.32}) \times 10^{-5}$	0.013	0.000	0.036	0.004	0.015	-0.050	-0.014
150.4–168.7	158.9	$(3.43 \pm 0.05\,^{+0.14}_{-0.23}) \times 10^{-5}$	0.014	0.000	0.036	0.002	0.015	-0.051	-0.014
168.7–189.3	178.6	$(2.44 \pm 0.04\,^{+0.10}_{-0.16}) \times 10^{-5}$	0.014	0.000	0.036	0.001	0.015	-0.051	-0.015
189.3–212.4	200.1	$(1.66 \pm 0.03\,^{+0.07}_{-0.11}) \times 10^{-5}$	0.016	0.000	0.036	-0.000	0.015	-0.051	-0.015
212.4–238.3	224.6	$(1.17 \pm 0.02\,^{+0.05}_{-0.08}) \times 10^{-5}$	0.016	0.000	0.036	-0.001	0.015	-0.049	-0.015
238.3–267.4	252.0	$(8.04 \pm 0.19\,^{+0.34}_{-0.50}) \times 10^{-6}$	0.017	0.000	0.036	-0.001	0.014	-0.046	-0.016
267.4–300.0	282.6	$(5.60 \pm 0.15\,^{+0.24}_{-0.33}) \times 10^{-6}$	0.017	0.000	0.036	-0.001	0.014	-0.041	-0.016
300.0–336.6	317.3	$(3.89 \pm 0.12\,^{+0.17}_{-0.22}) \times 10^{-6}$	0.018	0.000	0.036	-0.001	0.013	-0.034	-0.017
336.6–377.7	355.3	$(2.71 \pm 0.09\,^{+0.12}_{-0.14}) \times 10^{-6}$	0.018	0.000	0.036	-0.000	0.013	-0.026	-0.018
377.7–423.8	399.2	$(1.82 \pm 0.07\,^{+0.08}_{-0.09}) \times 10^{-6}$	0.019	0.000	0.036	0.000	0.012	-0.016	-0.019
423.8–475.5	447.7	$(1.29 \pm 0.06\,^{+0.05}_{-0.06}) \times 10^{-6}$	0.019	0.000	0.036	0.001	0.012	-0.004	-0.021
475.5–598.6	529.0	$(7.46 \pm 0.22\,^{+0.32}_{-0.46}) \times 10^{-7}$	$^{+0.014}_{-0.045}$	0.000	0.036	0.001	0.011	0.016	-0.023
598.6–753.6	666.2	$(3.52 \pm 0.14\,^{+0.23}_{-0.28}) \times 10^{-7}$	$^{+0.019}_{-0.066}$	0.000	0.036	-0.001	0.009	0.050	-0.026
753.6–948.7	841.8	$(1.63 \pm 0.08\,^{+0.16}_{-0.14}) \times 10^{-7}$	$^{+0.021}_{-0.071}$	0.000	0.036	-0.007	0.008	0.090	-0.029
948.7–1194.3	1055.3	$(6.72 \pm 0.50\,^{+0.93}_{-0.54}) \times 10^{-8}$	$^{+0.026}_{-0.062}$	0.000	0.036	-0.019	0.007	0.130	-0.030
1194.3–1892.9	1454.7	$(1.59 \pm 0.14\,^{+0.30}_{-0.16}) \times 10^{-8}$	$^{+0.100}_{-0.075}$	0.000	0.036	-0.047	0.006	0.152	-0.024
1892.9–3000.0	2241.5	$(3.41 \pm 0.53\,^{+0.55}_{-0.58}) \times 10^{-9}$	$^{+0.038}_{-0.127}$	0.000	0.036	-0.106	0.009	0.152	0.008
3000.0–4754.7	3899.0	$(4.68\,^{+1.97}_{-1.38}\,^{+1.59}_{-1.39}) \times 10^{-10}$	$^{+0.273}_{-0.242}$	0.000	0.036	-0.169	0.020	0.152	0.126
4754.7–7535.7	5641.9	$(1.95\,^{+1.08}_{-0.72}\,^{+0.74}_{-0.92}) \times 10^{-10}$	$^{+0.193}_{-0.454}$	0.000	0.036	-0.127	0.036	0.152	0.286

FIT OF THE CALET RESULTS WITH DAMPE'S BINNING

In Fig. S5, we show the cosmic-ray all-electron spectrum measured by CALET using the same energy binning as DAMPE's result [S5] and compared with it. The error bars indicate the quadratic sum of statistical and systematic errors except the normalization uncertainty. As in our previous publication [S2], we fit the spectrum in the energy range from 55 GeV to 2630 GeV with a smoothly broken power law model defined as: $J(E) = C(E/100GeV)^{\gamma}(1 + (E/E_b)^{\Delta\gamma/s})^{-s}$, where E_b is the break energy, while γ is the power index below E_b and $\Delta\gamma$ is the difference in the power index below and above E_b. The cyan line represents the fit with E_b fixed at 914 GeV as determined by DAMPE [S5], yielding a steepening of the fitted spectrum from γ=-3.15±0.01 by $\Delta\gamma$=-0.97±0.20. The blue line shows a fit in which E_b is a free parameter, yielding a steepening of the fitted spectrum at energy E_b =599±173 GeV from γ=-3.12±0.03 by $\Delta\gamma$=-0.57±0.18. In both fits, the break smoothness parameter s is fixed at 0.1, and a good fit to our data is obtained, with χ^2/NDF = 17 / 25 and χ^2/NDF = 13 / 24, respectively. An exponentially cutoff power law [S4] (green line) with a power index of -3.03±0.02 below a cutoff energy of 1921±243 GeV also fits well, with χ^2/NDF = 15 / 25. In the given energy range and with DAMPE's binning, all these fits are favored at more than 6 σ over a single power-law fit, which gives an index -3.19±0.01 with χ^2/NDF = 59 / 26.

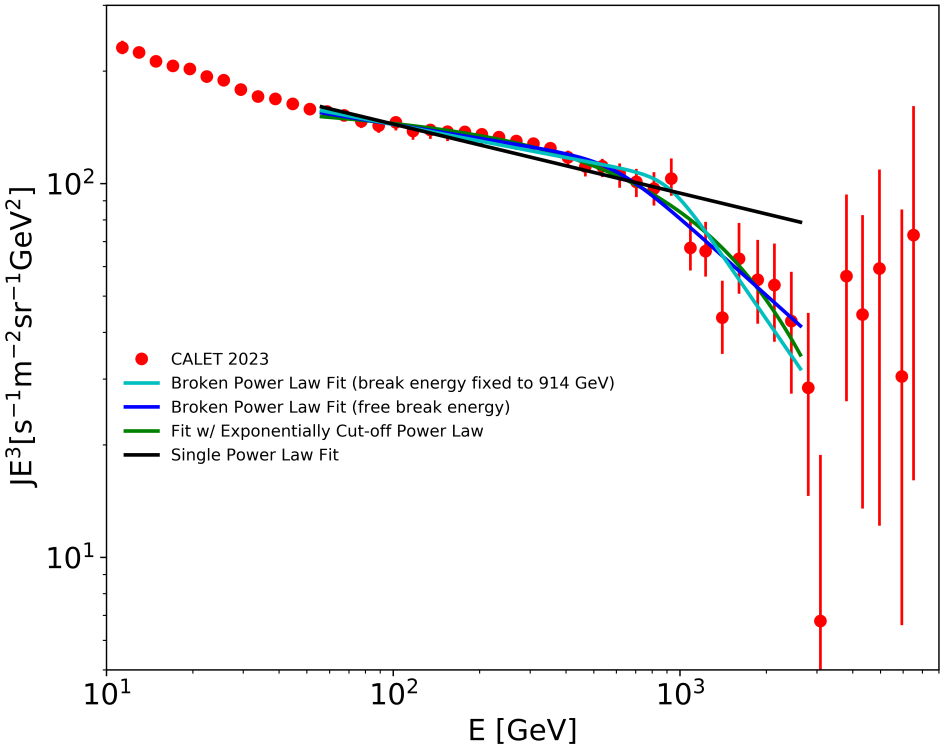

FIG. S5. All-electron spectrum measured by CALET with the binning used by DAMPE in Ref. [S5], and spectral fits in a restricted energy interval from 55 GeV to 2630 GeV as in our previous publication [S2] including a broken power law, an exponentially cutoff power law, and a single power law. The error bars represent statistical and systematic uncertainties except normalization. More details can be found in the text.

THE SPECTRUM FITTED WITHOUT CONTRIBUTION FROM NEARBY SNRs

In Fig. S6, we present the best fit over the whole region of the CALET all-electron spectrum and the AMS-02 positron data as in Fig. 4 of the main paper, but without the contribution from the three nearby SNRs. The fits with and without nearby sources give $\chi^2/\mathrm{NDF} = 34/80$ and $\chi^2/\mathrm{NDF} = 32/80$, respectively, showing that this model fits the data exceedingly well and neither case is significantly favored over the other. However, the fitting result above 4.8 TeV (7.5 TeV) predicts an excess of 11.0 (4.2) events with nearby sources and 4.6 (1.0) without nearby sources, respectively. An excess of 9 (4) events above 4.8 TeV (7.5 TeV) obtained by the event-by-event analysis described below is compatible with the expected contribution from nearby SNRs (mainly Vela).

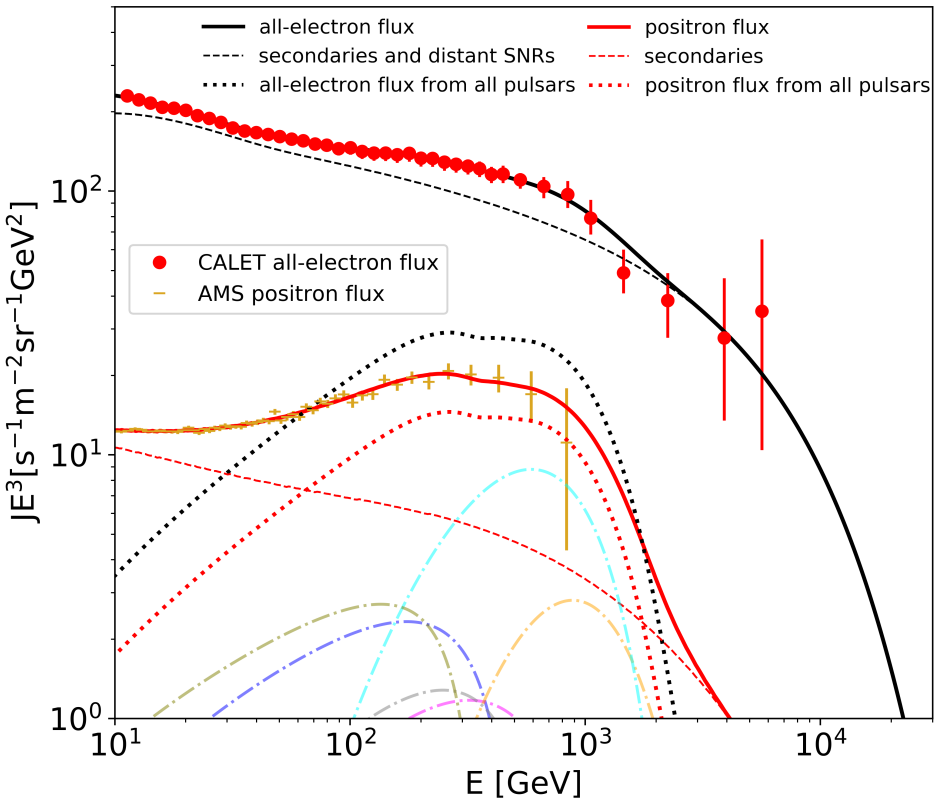

FIG. S6. Spectral fit over the whole region of the CALET all-electron observation and the AMS-02 positron data as in Fig.4, but without the contributions from nearby SNRs.

EVENT-BY-EVENT ANALYSIS: ELECTRON SELECTION WITH LIKELIHOOD ESTIMATION ON EACH EVENT

For better electron identification above 4.8 TeV, we applied an event-by-event analysis to select the electron candidates which are pre-selected by the BDT response distributions with 13 parameters. The analysis is carried out for each individual candidate event with a dataset of simulated electrons and protons generated under the same conditions of deposited shower energy, incident position, and arrival direction. The simulated electron dataset for each candidate contains 10^5 events thrown with the most likely primary energy to result in the same energy deposit as the candidate event. The simulated proton dataset for each candidate contains $2 \times 10^5 - 10^6$ events thrown with a power law distribution (index -2.7) over two orders of magnitude above the real energy deposit. The analysis procedure follows:

1. Filter the simulated datasets using the same pre-selection conditions as applied to the flight dataset in the generation of the candidate list (except for the final BDT selection).

2. Further filter the simulated proton dataset to only accept events with energy deposit within 50% of that for the real candidate event. Energy-deposit dependence of the selection parameters is evaluated (and found to be small) and scaled to the real candidate event's energy deposit.

3. Generate distributions of the 13 selection parameters for the simulated and filtered electron and proton datasets.

4. Generate distributions of likelihood ratio (LR) for the simulated electron and proton datasets according to

$$LR(k) = \log_{10} \prod_{i=1}^{n} \frac{p_e^{(k)}(i)}{p_p^{(k)}(i)} \tag{S1}$$

   for event k and selection parameter i (up to $n = 13$), such that

$$p_s^{(k)}(i) = \frac{m_s^{(k)}(i)}{m_s^{(tot)}(i)} \tag{S2}$$

   where $m_s^{(k)}(i)$ is the number of events in the same bin as event k of the histogram of selection parameter i for species s, and $m_s^{(tot)}(i)$ is the total number of events in that histogram.

5. Calculate the LR for the real candidate event in the same fashion, using the real observed values of the 13 selection parameters.

6. Scale the distributions of LR for the electron and proton distributions such that the ratio of protons to electrons matches that observed in the template fit of the pre-cut BDT parameters in the energy bin corresponding to the real candidate event.

7. Further scale the distributions of LR such that the sum of simulated electron events with LR equal to or above that of the real candidate event is equal to 1. After this scaling, the integral of the proton distribution with LR equal to or above that of the real candidate event provides the residual proton contamination probability p_{cont} for that candidate. That is to say, for each 1 electron in the electron dataset at the confidence level of the real candidate event, p_{cont} protons are observed.

8. In order to avoid underestimation of the proton background due to the paucity of proton events surviving at high values of LR, a Gaussian is fit to the tail of the distribution. The integral of this fit is used as a more conservative estimate of the proton contamination probability.

As an example, in Fig. S7, the LR distribution of an event with reconstructed energy 12.04 TeV and LR of 8.47 is compared with the distributions for the corresponding simulated electron and proton samples weighted by the BDT template fit as described above. Vertical lines indicate the values of LR such that 80% (dashed) and 50% (dotted) of the electron sample remain, and the LR for the real event (solid). The observed event has p_{cont} of 0.004, representing a less than 1% proton contamination probability. The shower profile projected to the X-Z and Y-Z planes is presented in Fig. S8.

By applying this likelihood analysis to all candidate events in the observation time covered by this work, we select 9 (4) events of the pre-selected 16 (8) events above 4.8 (7.5) TeV which have $p_{cont} < 0.1$.

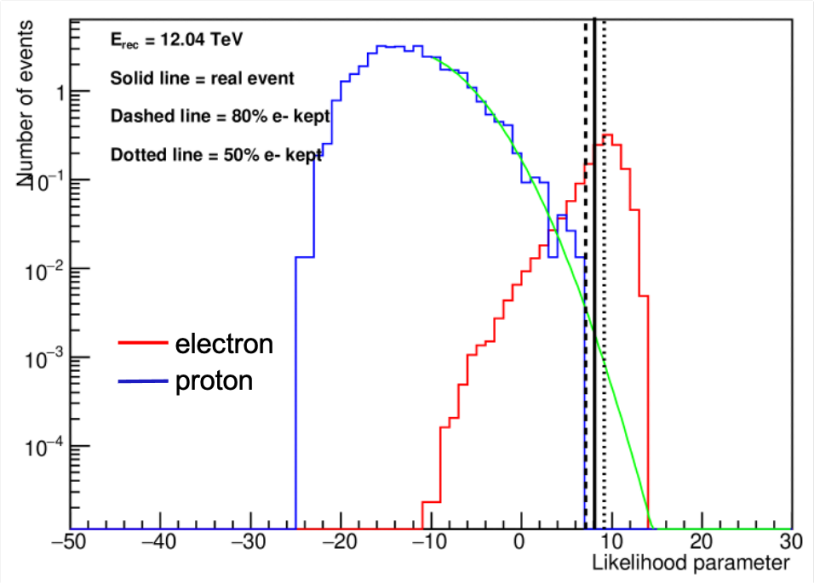

FIG. S7. Comparison of the LR of the observed event with energy 12.04 TeV with simulated LR distributions of electrons (red) and the corresponding background protons (blue). The green line is a Gaussian fit of the proton distribution tail. The solid vertical line presents the LR value of the observed event. The dashed line and the dotted line indicate the values of LR such that 80% and 50% of the electron sample remain, respectively.

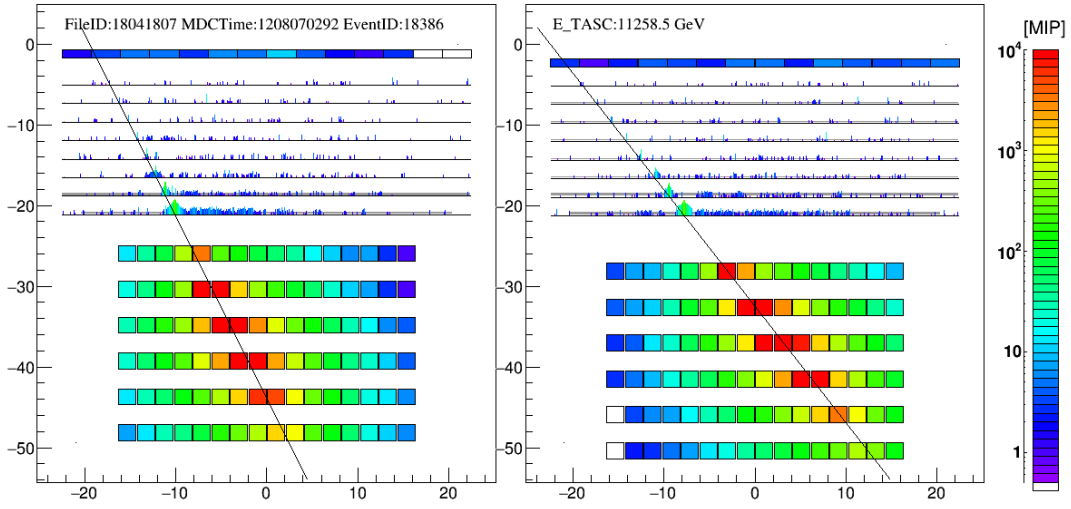

FIG. S8. The shower profiles projected onto the X-Z (left) and Y-Z (right) view of the high-energy electron event with an energy deposit sum in TASC of 11.26 TeV. Black lines represent the reconstructed tracks using the shower tracking [S6], which achieves a fine resolution taking advantage of the high granularity of the IMC.

[S1] See Supplemental Material at https://journals.aps.org/prl/supplemental/10.1103/PhysRevLett.120.261102 for supporting figures, which includes Ref. [S2].
[S2] O. Adriani *et al.* (CALET Collaboration), Phys. Rev. Lett. **120**, 261102 (2018).
[S3] M. Aguilar *et al.* (AMS-02 Collaboration), Phys. Rep. **894**, 1–116 (2021).
[S4] S. Abdollahi *et al.* (Fermi-LAT Collaboration), Phys. Rev. D **95** 082007 (2017).
[S5] G. Ambrosi *et al.* (DAMPE Collaboration), Nature **552**, 63–66 (2017).
[S6] Y. Akaike *et al.* in *Proceedings of 33rd International Cosmic Ray Conference (*ICRC2013) 726 (2013), https://articles.adsabs.harvard.edu/pdf/2013ICRC...33.2162A.